PAPER

Check for updates

Multi-electron excitation contributions towards primary and satellite states in the photoelectron spectrum†

Torsha Moitra, ‡[a] Alexander C. Paul, ‡[b] Piero Decleva, [c] Henrik Koch ⋆[bd] and Sonia Coriani ⋆[ab]

The computation of Dyson orbitals and corresponding ionization energies has been implemented within the equation of motion coupled cluster singles, doubles and perturbative triples (EOM-CC3) method. Coupled to an accurate description of the electronic continuum *via* a time-dependent density functional approach using a multicentric B-spline basis, this yields highly accurate photoionization dynamical parameters (cross-sections, branching ratios, asymmetry parameters and dichroic coefficients) for primary (1h) states as well as satellite states of (2h1p) character. Illustrative results are presented for the molecular systems H_2O, H_2S, CS, CS_2 and (*S*)-propylene oxide (a.k.a. methyloxirane).

1 Introduction

Significant advancements in high-resolution photoelectron spectroscopy have led to a renewed quest for accurate theoretical assignments, in particular of the high energy region of the photoelectron spectrum, comprising low intensity peaks.[1,2] Under the sudden approximation limit,[3] the photoelectron is assumed to be removed instantaneously from the system, without allowing for the other electrons to adjust to the hole potential. Under such circumstances, there is a finite probability of ionic state to be in its excited state, generating a satellite in the photoelectron spectrum. Starting from the initial state *N*-electron configuration, these satellite states are attributed to multi-electron excitations of 2h1p (two-hole one-particle) or higher order character.[4] The appearance of satellites in the theoretical spectra is guided by both correlation and relaxation effects, the former describing the multi-electron excitation character, whereas the latter accounts for the rearrangement of the orbitals around the ionized hole. However, these two effects are inseparable to a certain degree.[4–6]

For the theoretical description of the shake-up satellite states, a method capable of capturing many-body effects is thus required. Based on Koopmans theorem, only primary (1h) states are accessible. This "*breakdown of the molecular orbital picture*" in molecular photoionization due to correlation effects was pointed out decades ago, see *e.g.* the work of Cederbaum and collaborators.[4,7,8] Ever since, numerous efforts have been directed towards the development of theoretical methods that go beyond the simple Koopmans' picture of the process. The literature on the subject is vast and steadily growing. Without any ambition to give an exhaustive account, and starting from the correlated description of the bound states, we mention here various Green's function (GF) methods (see, *e.g.*, ref. 9 for a recent review) like the Dyson and non-Dyson variants of the Algebraic Diagrammatic Construction to third order (ADC3),[10–12] and the 'outer valence' GF approach (OVGF),[13] see also ref. 14; the symmetry-adapted-cluster configuration interaction general-R (SACCI-R) approach;[15,16] the Configuration Interaction (CI) method;[17] multiconfigurational approaches like complete active space self-consistent field (CASSCF),[18] restricted active space SCF (RASSCF) and CAS/RAS with a second-order perturbation theory (CASPT2/RASPT2).[5,6,19–24]

Popular correlated frameworks to compute molecular properties and spectra, including photoelectron spectra and photo-ionisation dynamical properties,[25–29] are coupled cluster response theory (CCRT)[30,31] and the equation of motion (EOM) coupled cluster method.[32–35] CCRT provides size-intensive excitation energies and transition moments;[30,31] EOM-CC[32–35] gives the same excitation energies as CCRT, but the transition moments are different and not strictly size-intensive. On the other hand, the computational cost of EOM

[a] *DTU Chemistry, Technical University of Denmark, DK-2800 Kongens Lyngby, Denmark. E-mail: soco@kemi.dtu.dk*

[b] *Department of Chemistry, NTNU – Norwegian University of Science and Technology, N-7491 Trondheim, Norway*

[c] *Istituto Officina dei Materiali IOM-CNR and Dipartimento di Scienze Chimiche e Farmaceutiche, Università degli Studi di Trieste, I-34121 Trieste, Italy*

[d] *Scuola Normale Superiore, I-56126 Pisa, Italy. E-mail: henrik.koch@sns.it*

‡ These authors contributed equally to this work.

This journal is © the Owner Societies 2022

Phys. Chem. Chem. Phys., 2022, **24**, 8329–8343 | **8329**

transition moments is less demanding than for CCRT and the size-intensity errors are expected to be small. We therefore here use equation of motion coupled cluster singles, doubles and perturbative triples (EOM-CC3)[36–40] ionization energies and corresponding Dyson orbitals[13,25,41–44] to represent such transitions. The 2h1p satellites are in principle also attainable at the EOM coupled cluster singles and doubles (EOM-CCSD)[25,27,32–34] level; however, their ionization energies can be rather over-estimated.[45] The triples' correction is the basic requirement for the precise calculation of both ionization energies and corresponding intensities. The square norms of the Dyson orbitals[13,41–43] are proportional to the intensities of the photo-electron spectrum. Thus, it can be considered that the satellite state borrows intensity from the primary states that are mixed into it, leading to a decrease in intensity of the primary ionized states. In some cases, especially for transition metal complexes,[46] it becomes difficult to distinguish between primary and satellite states.

The simulation of the individual-channel photoionization observables additionally requires an explicit description of the outgoing electron in conjunction with the bound state of the system. A popular strategy to evade this is to reconstruct the total cross-section from purely bound-state pseudo-spectral representations spanning over the post-ionization region using Stieltjes Imaging or Padé approximant techniques.[47–54] However, these techniques are limited by the lack of proper asymptotic boundary conditions, which are needed to compute individual channel photoionization observables.

Several strategies have been developed to account for the continuum electrons. A straightforward method is to use simple analytic functions like plane waves and Coulomb waves.[26] Though conceptually simple, these methods fail to reproduce complex phenomena like the appearance of Cooper minima or shape resonances.[27] More accurate approaches determine the continuum orbitals numerically using stationary conditions formulated within the *R*-matrix,[55,56] Schwinger variational,[57,58] complex Kohn[59] and least-square or Galerkin methods.[60,61] While grid methods can be easily implemented in one-center expansion (OCE) approaches,[62] current trend is to employ a multicenter basis set, with a long range OCE and a small number of additional functions centered on the nuclei, in the spirit of the linear combination of atomic orbitals (LCAO) approach. For the one center radial functions, B-splines[56,60,63,64] or similar finite elements[65] are popular. A hybrid approach joining short-range Gaussians and long-range B-splines overlapping over an intermediate interval has also been shown viable.[66,67] Gaussians or the same B-splines are used for the LCAO part.

As anticipated, we here present a study on the effect of the inclusion of triple excitations in the bound state description on both the primary and satellite ionized states. For this purpose, firstly the EOM-CC3 Dyson orbitals have been implemented in the e^T software package.[68] In order to account for the outgoing electron, multicentric B-spline time-dependent density functional theory is used.[45] The Dyson orbitals are utilized not only to estimate the intensities in the photoelectron spectra, but first and foremost to compute the single-particle photoelectron

matrix elements needed to obtain the photoionization observables.[5,25,27]

In Section 2, we detail the composite theoretical approach, with emphasis on the implementation of the EOM-CC3 Dyson orbital. The computational protocol used is described in Section 3. In Section 4, the devised formalism is validated by studying the valence ionization dynamics of simple molecules like H_2O, H_2S, CS, CS_2 and (*S*)-C_3H_6O. Emphasis on the inner valence region of the spectra is given due to the presence of multiple closely-lying ionized states of substantial 2h1p nature. Comparison of CCSD and CC3 coupled to TD-DFT for the bound and continuum part, respectively, has been presented wherever deemed meaningful. Section 5 summarizes our findings.

2 Theory

The key quantity encapsulating all the information of the initial (Ψ_i^N) and final composite state (Φ_f) of the system is given by the photoelectron matrix element,

$$D^{\text{if}} = \langle \Psi_i^N | \vec{d} | \Phi_f \rangle. \tag{1}$$

In eqn (1), $\vec{d}$ is the electric dipole moment. The most general approach is to expand Φ_f in a CI-type fashion, called the "close-coupling" form.[69] A number of close-coupling implementations are available, and can give accurate results for small molecules, especially close to threshold.[56,58,66,67] However, *ab initio* computations using the full expansion are computationally expensive and often unnecessary. We have restricted ourselves to the single channel approximation, where the final composite state is represented by the anti-symmetrized product of the photoelectron and the bound ionized state accessible at that particular energy

$$\Phi_f \equiv \Phi_{EI\alpha} = \mathscr{A}(\Psi_I^{N-1} \phi_{EI\alpha}). \tag{2}$$

Under these assumptions, the photoelectron matrix element in eqn (1) boils down to a single particle photoelectron matrix element, given by

$$D^{\text{if}} = \langle \phi_{\text{if}}^D | \vec{d} | \phi_{EI\alpha} \rangle. \tag{3}$$

All information about the bound initial *N*-electron and final (*N* − 1)-electron states is now compressed into the orbital function ϕ_{if}^D, called the Dyson orbital.[41–43] From now onward, we will drop the suffix *if* from ϕ_{if}^D. For details on how to obtain the above simplified expression, we refer to, *e.g.*, ref. 45 and the supplementary information file of ref. 27.

2.1 EOM-CC3 Dyson orbitals

The coupled cluster (CC) wave function is defined by

$$|\text{CC}\rangle = e^T |\text{HF}\rangle, \quad T = \sum_\mu t_\mu X_\mu, \tag{4}$$

where the cluster operator T is composed of the excitation operator X_μ and the amplitudes t_μ. The excitation operator consists of strings of singlet excitation operators, E_{ai}, and maps the Hartree–Fock determinant into excited determinants $|\mu\rangle$.

8330 | *Phys. Chem. Chem. Phys.*, 2022, **24**, 8329–8343

This journal is © the Owner Societies 2022

We use the standard notation where indices i, j, k,... refer to occupied, a, b, c,... to virtual, and p, q, r,... to general orbitals. The hierarchy of coupled cluster methods is obtained by truncating the cluster operator at a certain number of excitations.[70] We introduce the similarity transformed Hamiltonian,

$$\bar{H} = e^{-T}He^{T}, \tag{5}$$

where the electronic (spin-free) Hamiltonian, H, in second quantization is defined as[70]

$$H = \sum_{pq} h_{pq}E_{pq} + \frac{1}{2}\sum_{pqrs} g_{pqrs}(E_{pq}E_{rs} - E_{ps}\delta_{rq}). \tag{6}$$

The amplitudes are obtained by solving the projected coupled cluster equations[70]

$$\langle\mu|\bar{H}|\mathrm{HF}\rangle = \Omega_\mu = 0, \tag{7}$$

and the energy is given as

$$E_{\mathrm{CC}} = \langle\mathrm{HF}|\bar{H}|\mathrm{HF}\rangle. \tag{8}$$

The projection space is generated by the contravariant excitation operator, $\tilde{X}_\mu$, such that the determinants are biorthogonal to the determinants created by the cluster operator

$$\langle\mu| = \langle\mathrm{HF}|\tilde{X}_\mu, \quad |\nu\rangle = X_\mu|\mathrm{HF}\rangle, \quad \langle\mu|\nu\rangle = \delta_{\mu,\nu}. \tag{9}$$

In EOM-CC theory,[32] additional operators, L_m and R_m, are introduced that generate the m-th EOM states, $\langle L_m|$ and $|R_m\rangle$:

$$L_m = l_0^m + \sum_\mu L_\mu^m \tilde{X}_\mu \tag{10}$$

$$\langle L_m| = \left(\langle\mathrm{HF}|l_0^m + \sum_\mu \langle\mu|L_\mu^m\right)e^{-T} \tag{11}$$

$$R_m = r_0^m + \sum_\mu R_\mu^m X_\mu \tag{12}$$

$$|R_m\rangle = e^T\left(r_0^m|\mathrm{HF}\rangle + \sum_\mu R_\mu^m|\mu\rangle\right) \tag{13}$$

The additional parameters are determined as left and right eigenvectors of the similarity transformed Hamiltonian

$$\bar{\mathbf{H}}^T \boldsymbol{L}_m = E_m \boldsymbol{L}_m \tag{14}$$

$$\bar{\mathbf{H}} \boldsymbol{R}_m = E_m \boldsymbol{R}_m, \tag{15}$$

where the eigenvalue, E_m, corresponds to the total energy of the state. Assuming that the ground state equations have been solved, the Hamiltonian matrix has the following form

$$\bar{\mathbf{H}} = \begin{pmatrix} E_{\mathrm{CC}} & \boldsymbol{\eta}^T \\ \mathbf{0} & \mathbf{J} + E_{\mathrm{CC}}\mathbf{I} \end{pmatrix}, \tag{16}$$

where $\mathbf{J}$ is the Jacobian, $J_{\mu\nu} = \langle\mu|[\bar{H},X_\nu]|\mathrm{HF}\rangle$ (also known as $\mathbf{A}$) and $\eta_\nu = \langle\mathrm{HF}|[\bar{H},X_\nu]|\mathrm{HF}\rangle$. From the structure of the Hamiltonian

matrix and the biorthonormality of the states, we find the left and right ground state solutions

$$\langle L_0| = \langle\widetilde{\mathrm{CC}}| = \left(\langle\mathrm{HF}| + \sum_\mu \langle\mu|\lambda_\mu\right)e^{-T} \tag{17}$$

$$|R_0\rangle = |\mathrm{CC}\rangle = e^T|\mathrm{HF}\rangle, \tag{18}$$

where the multipliers, λ_μ, are determined from $\boldsymbol{\lambda}^T\mathbf{J} = -\boldsymbol{\eta}$. The excited states are obtained as

$$\langle L_m| = \sum_\mu \langle\mu|L_\mu e^{-T} \tag{19}$$

$$|R_m\rangle = e^T\left(r_0|\mathrm{HF}\rangle + \sum_\mu R_\mu|\mu\rangle\right), \tag{20}$$

where m is larger than 0 and the superscript was removed from the amplitudes for simplicity. The parameter r_0 is defined as $r_0 = -\sum_\mu \lambda_\mu R_\mu$ to ensure biorthogonality to the left ground state, $\langle\widetilde{\mathrm{CC}}|$. Transition properties for a one-electron operator (in second quantization) $\mathcal{O} = \sum_{pq}\mathcal{O}_{pq}E_{pq}$ are given as biorthogonal expectation values,

$$\mathcal{O}_{0,m} = \langle\widetilde{\mathrm{CC}}|\mathcal{O}|R_m\rangle\langle L_m|\mathcal{O}|\mathrm{CC}\rangle \tag{21}$$

expressed in terms of transition densities

$$\tilde{D}_{pq}^{0-m} = \langle\widetilde{\mathrm{CC}}|E_{pq}|R_m\rangle \tag{22}$$

$$D_{pq}^{m-0} = \langle L_m|E_{pq}|\mathrm{CC}\rangle. \tag{23}$$

In order to obtain the CC3 equations, we divide the Hamiltonian into a one-particle operator (F) and a fluctuation potential (U),

$$H = F + U. \tag{24}$$

The single excitation amplitudes are considered zeroth order parameters as they are crucial for orbital relaxation, while double and triple excitation amplitudes are first and second order in the perturbation, U, respectively. Introducing the perturbation expansion into the expression for the energy of the EOM states,

$$E_m = \boldsymbol{L}_m^T\bar{\mathbf{H}}\boldsymbol{R}_m \tag{25}$$

and neglecting terms of fifth order and higher, yields the CC3 equations. Details about the derivation of the explicit terms and their implementation can be found in ref. 37, 38 and 40.

In EOM CC theory, ionization energies can be rigorously obtained by replacing the singlet excitation operators, $\tilde{X}_\mu$ and X_μ, in eqn (10) and (12) by particle nonconserving excitation operators like 1h, 2h1p,... operators, which defines the EOM-CC method for ionization potentials, EOM-IP-CC.[33] However, as proposed by Stanton and Gauss,[71] we can also compute the ionization energies by including a bath orbital in the virtual

This journal is © the Owner Societies 2022

Phys. Chem. Chem. Phys., 2022, **24**, 8329–8343 | **8331**

orbital space which does not interact with the other orbitals, and then projecting out all excitations that do not include the bath orbital during the solution of the eigenvalue equation.[72] This approach has the advantage of requiring only a small modification to an existing EOM-CC code for excitation energies (EOM-EE-CC). As a disadvantage, its scaling is the same as EOM-CC for excitation energies, whereas a rigorous implementation of EOM-IP-CC scales one order less with the number of virtual orbitals (n_v).

Dyson orbitals can be described as the overlap between a N-electron wave function and a $(N − 1)$-electron wave function.[13,25,41,42] Expressing a Dyson orbital, ϕ^D, in terms of molecular orbitals, ϕ_p, gives

$$\phi^D = \sum_p \gamma_p \phi_p, \tag{26}$$

where the expansion coefficients are defined as

$$\gamma_p = \langle \Psi^{N-1} | a_p | \Psi^N \rangle \tag{27}$$

for general $(N − 1)$ and N electron states, Ψ^{N-1} and Ψ^N. The squared norm of the Dyson orbital is called the pole strength, R_F,

$$R_F = \sum_p |\gamma_p|^2 \tag{28}$$

which is related to the intensity of the bands in the photoelectron spectrum. As coupled cluster is a non-Hermitian theory, two Dyson orbitals are obtained corresponding to the left and right ionized state for a given ionization potential

$$\gamma_p^L = \langle L_m | a_p | \mathrm{CC} \rangle; \tag{29}$$

$$\gamma_p^R = \langle \widetilde{\mathrm{CC}} | a_p^\dagger | R_m \rangle. \tag{30}$$

In analogy to the EOM-CC transition strength,[73,74] we define the pole strength as[27,45]

$$R_F = \sum_p \langle L_m | a_p | \mathrm{CC} \rangle \langle \widetilde{\mathrm{CC}} | a_p^\dagger | R_m \rangle. \tag{31}$$

Due to the biorthonormality of the EOM states, the pole strength assumes values between zero and one, while the norms of individual left and right Dyson orbitals depend on the norm of the corresponding ionized states, which can be significantly larger than one. If b denotes the bath orbital, eqn (29) and (30) can be rewritten as

$$\gamma_p^L = \langle L_m | E_{bp} | \mathrm{CC} \rangle \tag{32}$$

$$\gamma_p^R = \langle \widetilde{\mathrm{CC}} | E_{pb} | R_m \rangle. \tag{33}$$

These expressions demonstrate that the left/right Dyson orbitals can be obtained as the row/column corresponding to the bath orbital of the EOM CC transition densities D^{m-0} and $\tilde{D}^{0-m}$.[25] As the bath orbital is part of the virtual orbital space, only two of the four blocks of D^{m-0} and $\tilde{D}^{0-m}$ need to be constructed. Additionally, the ground state amplitudes t and multipliers λ are zero if one of their indices corresponds to the

bath orbital. Therefore, the CC3 contribution to the right Dyson orbital consists of only four terms, and there is only a single term for the left Dyson orbital. We list these additional terms as follows (where we also use the symbol += to highlight that these terms are added to the CCSD-like ones):

$$\gamma_k^R \mathrel{+}= \frac{1}{2} \sum_{\substack{ab\\ij}} \lambda_{ij}^{ab} \left(R_{ijk}^{abb} - R_{ikj}^{abb} \right) - \frac{1}{2} \sum_{\substack{abc\\ijl}} \lambda_{ijl}^{abc} t_{jk}^{bc} R_{il}^{ab}$$
$$- \frac{1}{4} \sum_{\substack{ab\\ijl}} \lambda_{ijl}^{abc} t_{ijk}^{abc} R_l^b \tag{34}$$

$$\gamma_c^R \mathrel{+}= \frac{1}{4} \sum_{\substack{ab\\ij}} \lambda_{ijk}^{abc} R_{ijk}^{abb} \tag{35}$$

$$\gamma_c^L \mathrel{+}= \frac{1}{2} \sum_{\substack{ab\\ij}} L_{ijk}^{abb} t_{ijk}^{abc} \tag{36}$$

The CC3 ionization energies and Dyson orbitals have been implemented in a development version of the e^T program package[68] using a bath orbital. The bath orbital is added to the virtual space after the Hartree–Fock step and its corresponding integrals are set to zero. For a description of the algorithms to solve for the ground state, the excited states and transition densities we refer to ref. 40.

Table S1 (ESI†) summarizes the scaling per iteration to obtain the ground state amplitudes, t and λ, the excited state parameters, L and R, as well as the cost per left/right Dyson orbital as implemented in e^T. In the current implementation, the Jacobian transformation of a trial vector is carried out in a triple loop over the occupied indices i, j, k. This allows us to use the full permutational symmetry of the triples amplitudes while keeping a dense block of the virtual indices for efficient matrix–matrix multiplications.[75,76] For the ionized states this algorithm computes some unnecessary terms scaling as $8n_v^4 n_o^3$ floating point operations (FLOP), because all amplitudes L_μ and R_μ that do not involve the bath orbital are zero. Switching to a loop over the virtual orbitals the scaling for the ionized states could be reduced to $8n_v^3 n_o^3$ FLOP. However, the computation of the ground state parameters and the left Dyson orbitals would still scale as shown in Table S1 (ESI†) and the cost for the right Dyson orbitals could only be reduced to $6n_v^4 n_o^3$ FLOP. For large systems and if many ionized states are requested, the savings would be significant, but for the systems considered in this work the scaling was not an issue and the optimization of the code is deferred.

2.2 Multicentric B-spline TD-DFT

In order to describe continuum orbitals, conventional $\mathscr{L}^2$ Gaussian type or Slater type orbitals are not very accurate, despite efforts to adapt them.[77–79] Instead, we use a highly flexible linear combination of primitive B-spline functions (ζ),

$$\zeta_{jlm}(r, \theta, \phi) = \frac{1}{r} B_j(r) Y_{lm}(\theta, \phi). \tag{37}$$

8332 | *Phys. Chem. Chem. Phys.*, 2022, **24**, 8329–8343

This journal is © the Owner Societies 2022

Within the Kohn–Sham (KS) static-exchange DFT approach, the Schrödinger equation has the form,

$$H_{KS}\phi_i = \varepsilon_i\phi_i; \quad i = 1, 2, \ldots, n \qquad (38)$$

where,

$$H_{KS} = -\frac{1}{2}\nabla^2 - \sum_M \frac{Z_M}{|\vec{r} - \vec{R}_M|} + \int\frac{\rho(\vec{r}')d\vec{r}'}{|\vec{r} - \vec{r}'|} + V_{XC}[\rho]. \qquad (39)$$

In the above expressions, ρ is the ground state electron density obtained from a preliminary conventional SCF calculation, Z_M and $\vec{R}_M$ are the atomic number and nuclear coordinate, respectively. V_{XC} is the exchange–correlation potential. As previously shown, the LB94 functional outperforms the LDA or GGA functionals for simulating KS photoionization, due to the correct asymptotic Coulomb behaviour.[80] The continuum KS orbitals are then extracted as the eigenfunctions of the Hamiltonian in eqn (39), with given positive eigenvalue equal

to the kinetic energy (E) of the photoelectron. The problem is recast as to obtain the eigenvectors (c) with a minimum modulus eigenvalue (a) of the energy-dependent matrix $\mathbf{A}^\dagger\mathbf{A}(E)$,

$$\mathbf{A}^\dagger\mathbf{A}(E)c = ac, \quad \mathbf{A}(E) = \mathbf{H} - E\mathbf{S}, \qquad (40)$$

where $\mathbf{H}$ and $\mathbf{S}$ are the Hamiltonian and overlap matrices, respectively.[64,81]

The natural extension of the KS-DFT approach to include interchannel coupling effects while still restricting the bound states to a single determinant representation is the TD-DFT method within the linear response formalism. The linear response of the electron density ($\delta\rho$) due to an external potential is evaluated following the scheme by Zangwill and Soven.[82] The effective self-consistent field potential (V^{SCF}) is the sum of the external potential (μ_{ext}) and Coulomb and exchange–correlation screening. Using the adiabatic local density approximation (ALDA)[82] for the exchange–correlation

Table 1 H$_2$O. Comparison of ionization energies (IE, in eV) and pole strengths. Experimental results are taken from ref. 89. The percentage of singles character (%|R_1|) in the right EOM-CCSD ionization vectors is given in parenthesis beside the computed IEs. The notation $i^{-1}(j^{-1}a)$ is used to specify, respectively, the ionization and the excitation (in parenthesis) components of the 1p transitions (where i, j and a indicate specific molecular orbitals). Only configurations having amplitudes R_i^b and R_{ij}^{ba} greater than 0.3 and 0.4, respectively, are listed. The HF ground-state electronic configuration is $1a_1^2 2a_1^2 1b_2^2 3a_1^2 1b_1^2$

	EOM-CCSD/aug-cc-pVTZ			EOM-CC3/aug-cc-pVTZ			Exp[89]
Peak	IE (%|R_1|)	R_F	Dominant amplitudes	IE	R_F	Dominant amplitudes	IE (intensity)
X $^2B_1$	12.62 (95%)	0.9149	$1b_1^{-1}$	12.67	0.8839	$1b_1^{-1}$	12.20
A $^2A_1$	14.83 (96%)	0.9155	$3a_1^{-1}$	14.89	0.8838	$3a_1^{-1}$	15.00
B $^2B_2$	19.00 (97%)	0.9250	$1b_2^{-1}$	19.04	0.8990	$1b_2^{-1}$	18.51
				26.09	0.0076	$1b_1^{-2}4a_1$, $1b_1^{-2}6a_1$	
				26.11	0.0034	$3a_1^{-1}(1b_1^{-1}4a_1)$, $1b_1^{-1}(3a_1^{-1}4a_1)$	
				27.70	0.0019	$1b_1^{-1}(3a_1^{-1}4a_1)$, $3a_1^{-1}(1b_1^{-1}4a_1)$	
				29.88	0.0066	$1b_1^{-1}(3a_1^{-1}5a_1)$, $3a_1^{-1}(1b_1^{-1}5a_1)$	
				30.02	0.0121	$3a_1^{-1}(1b_1^{-1}2b_1)$, $1b_1^{-1}(3a_1^{-1}2b_1)$	
				30.33	0.0143	$1b_1^{-2}2b_1$	
				30.68	0.0025	$1b_1^{-2}2b_1$, $3a_1^{-1}(1b_1^{-1}4a_1)$	
				30.73	0.0654	$1b_1^{-2}4a_1$	
				30.80	0.0081	$3a_1^{-2}4a_1$, $3a_1^{-2}6a_1$	
	32.80 (72%)	0.6876	$2a_1^{-1}$	31.93	0.1327	$2a_1^{-1}$, $1b_1^{-1}(3a_1^{-1}2b_1)$, $3a_1^{-1}(1b_1^{-1}2b_1)$	32.20 (0.58)
				32.08	0.0017	$1b_2^{-1}(3a_1^{-1}4a_1)$, $1b_2^{-1}(3a_1^{-1}6a_1)$	
				32.09	0.0021	$1b_2^{-1}(1b_1^{-1}4b_2)$, $3a_1^{-1}(1b_1^{-1}5a_1)$	
				32.22	0.0093	$1b_1^{-1}7a_1$	
				32.58	0.3024	$2a_1^{-1}$, $1b_1^{-1}(3a_1^{-1}2b_1)$	
				32.60	0.0013	$1b_1^{-1}(3a_1^{-1}4a_1)$, $3a_1^{-1}(1b_1^{-1}4a_1)$	
				32.96	0.0017	$3a_1^{-1}(1b_1^{-1}3b_1)$, $1b_1^{-1}(3a_1^{-1}3b_1)$	
				33.45	0.0771	$2a_1^{-1}$, $1b_1^{-2}8a_1$	
				33.47	0.0124	$1b_1^{-1}$, $1b_1^{-1}(1b_2^{-1}5a_1)$, $1b_1^{-2}3b_1$	
				34.33	0.0133	$1b_2^{-1}$, $1b_2^{-1}(1b_1^{-1}2b_1)$, $1b_1^{-1}(1b_2^{-1}2b_1)$	
				34.50	0.0353	$2a_1^{-1}$, $3a_1^{-2}4a_1$, $1b_2^{-1}(3a_1^{-1}5a_1)$	
				34.87	0.0089	$3a_1^{-2}5a_1$	
	35.14 (17%)	0.1526	$2a_1^{-1}$, $1b_1^{-2}6a_1$	35.05	0.0155	$2a_1^{-1}$, $1b_1^{-1}(3a_1^{-1}3b_1)$, $3a_1^{-1}(1b_1^{-1}3b_1)$	35 (0.18)
				35.07	0.0012	$1b_2^{-1}(1b_1^{-1}5a_1)$, $1b_1^{-1}(3a_1^{-1}8a_1)$	
				35.59	0.0112	$2a_1^{-1}$, $3a_1^{-2}4a_1$	
				35.78	0.0058	$1b_2^{-1}(1b_1^{-1}2b_1)$, $1b_1^{-1}(1b_2^{-1}2b_1)$	
				35.93	0.0471	$2a_1^{-1}$, $3a_1^{-1}(1b_2^{-1}5a_1)$, $1b_1^{-2}9a_1$	
				36.14	0.0358	$2a_1^{-1}$, $1b_1^{-2}9a_1$	
				36.15	0.0043	$1b_2^{-1}(3a_1^{-1}5a_1)$, $3a_1^{-1}(1b_2^{-1}5a_1)$	
				36.45	0.0049	$2a_1^{-1}$, $1b_1^{-1}(1b_2^{-1}1a_2)$, $1b_2^{-1}(1b_1^{-1}1a_2)$	
				36.62	0.0025	$1b_2^{-1}(1b_1^{-1}3b_2)$, $1b_1^{-1}(1b_2^{-1}5a_1)$	

This journal is © the Owner Societies 2022

Phys. Chem. Chem. Phys., 2022, **24**, 8329–8343 | **8333**

kernel, the effective potential becomes,

$$V^{\text{SCF}}(\bar{r}, \omega) = \mu_{\text{ext}}(\bar{r}, \omega) + \int \frac{\delta\rho(\bar{r}', \omega)\mathrm{d}\bar{r}'}{|\bar{r} - \bar{r}'|} + \frac{\partial V_{\text{XC}}}{\partial \rho}\bigg|_{\rho(\bar{r})} \delta\rho(\bar{r}, \omega).$$
(41)

The response density is obtained from the KS dielectric susceptibility (χ) and the effective potential as,

$$\delta\rho(\bar{r}, \omega) = \int \chi(\bar{r}, \bar{r}', \omega) V^{\text{SCF}}(\bar{r}, \omega)\mathrm{d}\bar{r}'.$$
(42)

Inserting eqn (42) in eqn (41) gives the integral equation,

$$V^{\text{SCF}}(\bar{r}, \omega) = \mu_{\text{ext}}(\bar{r}, \omega) + \iint \kappa(\bar{r}, \bar{r}')\chi(\bar{r}', \bar{r}'', \omega) \times V^{\text{SCF}}(\bar{r}'', \omega)\mathrm{d}\bar{r}'\mathrm{d}\bar{r}''$$
(43)

where,

$$\kappa(\bar{r}, \bar{r}') = \frac{1}{|\bar{r} - \bar{r}'|} + \delta(\bar{r} - \bar{r}')\frac{\partial V_{\text{XC}}}{\partial \rho}.$$
(44)

Eqn (43) is solved with respect to V^{SCF}, avoiding the need for a self-consistent procedure.[64]

2.3 Photoionization observables

Once the Dyson orbitals and the continuum orbitals are known, all photoionization parameters can be computed. The photoelectron matrix element (eqn (3)) is related to the differential photoionization cross-section

$$\frac{\mathrm{d}\sigma}{\mathrm{d}\vec{k}} = 4\pi^2\alpha\omega|D^{\text{if}}|^2,$$
(45)

where α is the fine structure constant, ω is the photon energy and $\vec{k}$ is the momentum of the photoelectron in the molecular frame. Following the mathematical manipulations proposed by Chandra,[83] one obtains

$$\frac{\mathrm{d}\sigma}{\mathrm{d}\vec{k}} = \frac{\sigma}{4\pi}\left[1 + \left(-\frac{1}{2}\right)^{|m_{\text{r}}|}\beta P_2(\cos\theta) + m_{\text{r}}\beta_1 P_1(\cos\theta)\right].$$
(46)

It is evident from eqn (46) that the angular distribution of the photoelectron is guided by three parameters, namely the partial cross-section (σ), the asymmetry parameter (β) and the photoelectron dichroic parameter (β_1). The light polarization, m_{r}, can have values 0 (linearly polarized light), +1 (left circularly polarized light) and −1 (right circularly polarized light); P_i are the Legendre polynomials of order i and θ is the angle between the photoelectron moment and the light polarization, for linear polarization, or light propagation, for circular polarization. Additionally, we report the branching ratio, which is defined as the ratio between the partial photoionization cross-section of an individual channel and the sum of the partial cross-sections of all ionization channels considered.

3 Computational details

Experimental geometries from the NIST database[84] have been used for H_2O, H_2S, CS and CS_2. The geometry of (S)-methyloxirane was taken from a previous work.[85] The Dyson orbitals were obtained from the e^T program package[68] using the aug-cc-pVTZ basis set for H_2O, H_2S, CS and (S)-methyloxirane and the aug-cc-pVDZ set for CS_2. The ground state electronic densities were computed with the ADF software,[86] using the LB94 exchange–correlation functional and DZP basis set.[87] Occupied and continuum orbitals were obtained solving eqn (38) in a basis of B-spline functions. A long range expansion of the B-spline functions with angular momentum $L_{\max}$ is placed at the origin of the coordinate system (center of mass), up to a maximum radial grid length of $R_{\max}$ with n_{step} grid points. Additional off-center functions were placed on the non-center atoms with an angular momentum of $l_{\max}$ and radial grid length of $r_{\max}$. The parameters used are listed in Table S2 (ESI†). This choice of parameters ensured accurate convergence of the photoionization observables. The projected bound (Dyson) and continuum orbitals on the multicentric B-spline basis, and finally the photoionization observables were obtained using the Tiresia code.[63] Dyson orbital plots were prepared with UCSF ChimeraX.[88]

4 Results and discussions

4.1 Water

We start by showcasing the applicability and performance of our implementation of the EOM-CC3 ionization energy and Dyson orbitals in the case of the H_2O molecule. The importance
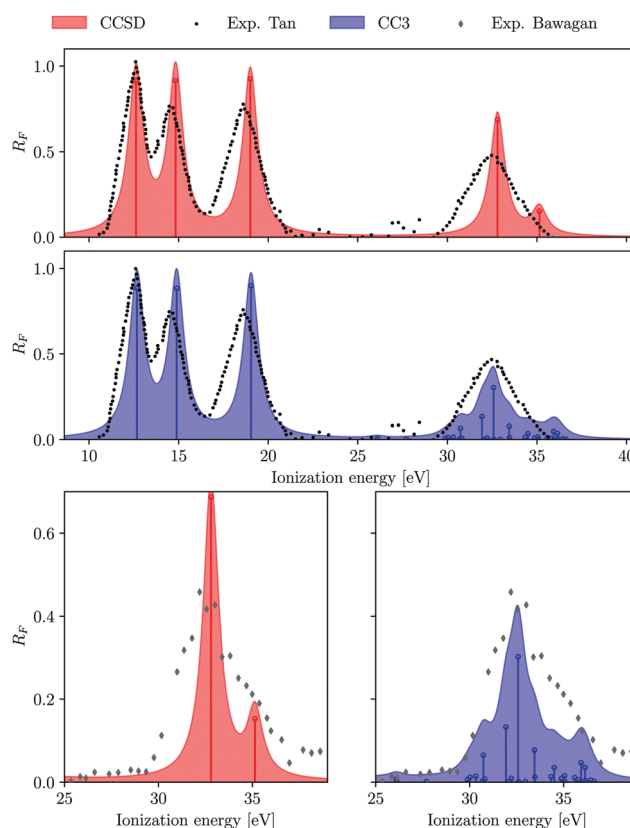

Fig. 1 H_2O. Comparison of experimental and computed photoelectron spectrum. Experimental results are taken from ref. 90 and 89.

of incorporating triple excitations is evaluated for the outer and inner valence regions of the photoelectron spectrum.

A comparison of the ionization energies and spectral strengths computed at EOM-CCSD and EOM-CC3 level is reported in Table 1, with details on the dominant amplitudes and percentage of singles character ($\%|R_1|$) in the right ionization vectors. Fig. 1 is a rendering of the photoelectron spectrum of each method based on the tabulated data, compared *vis-à-vis* with experimental data from ref. 90 for the whole spectrum, and from ref. 89 for the inner region satellite. The three lowest ionization energies correspond to primary ionizations, characterised by electron ejection from a particular molecular orbital. The corresponding Dyson orbitals are also equivalent to the dominant molecular orbital. No significant difference in ionization energy is observed upon inclusion of the perturbative triples excitations. However, a consistent decrease in pole strengths R_F is reported at the EOM-CC3 level, in comparison

to EOM-CCSD. This gives way for redistribution of the intensity among satellite peaks.

In the experiment,[89] three peaks were identified in the inner valence region at 32.2, 35.0 and 38.9 eV, with the last one being an order of magnitude weaker than the first two. We have computed the ionization spectrum of H_2O up to 37 eV using both EOM-CCSD and EOM-CC3 methods, in order to characterise the first two satellite bands. As envisaged, the inner valence ionization region comprises more low intensity peaks at the EOM-CC3 level, *versus* only two peaks obtained at the EOM-CCSD level (at 32.80 and 35.14 eV). The two ionized states obtained at the EOM-CCSD level have corresponding Dyson orbitals with major contribution from the $2a_1$ molecular orbital.

The corresponding $2a_1$ Hartree–Fock/aug-cc-pVTZ molecular orbital energy is 36.82 eV. Somewhat surprisingly, the energies of these two EOM-CCSD ionizations agree well with the experimental observation. Nevertheless, the spectral strength of the
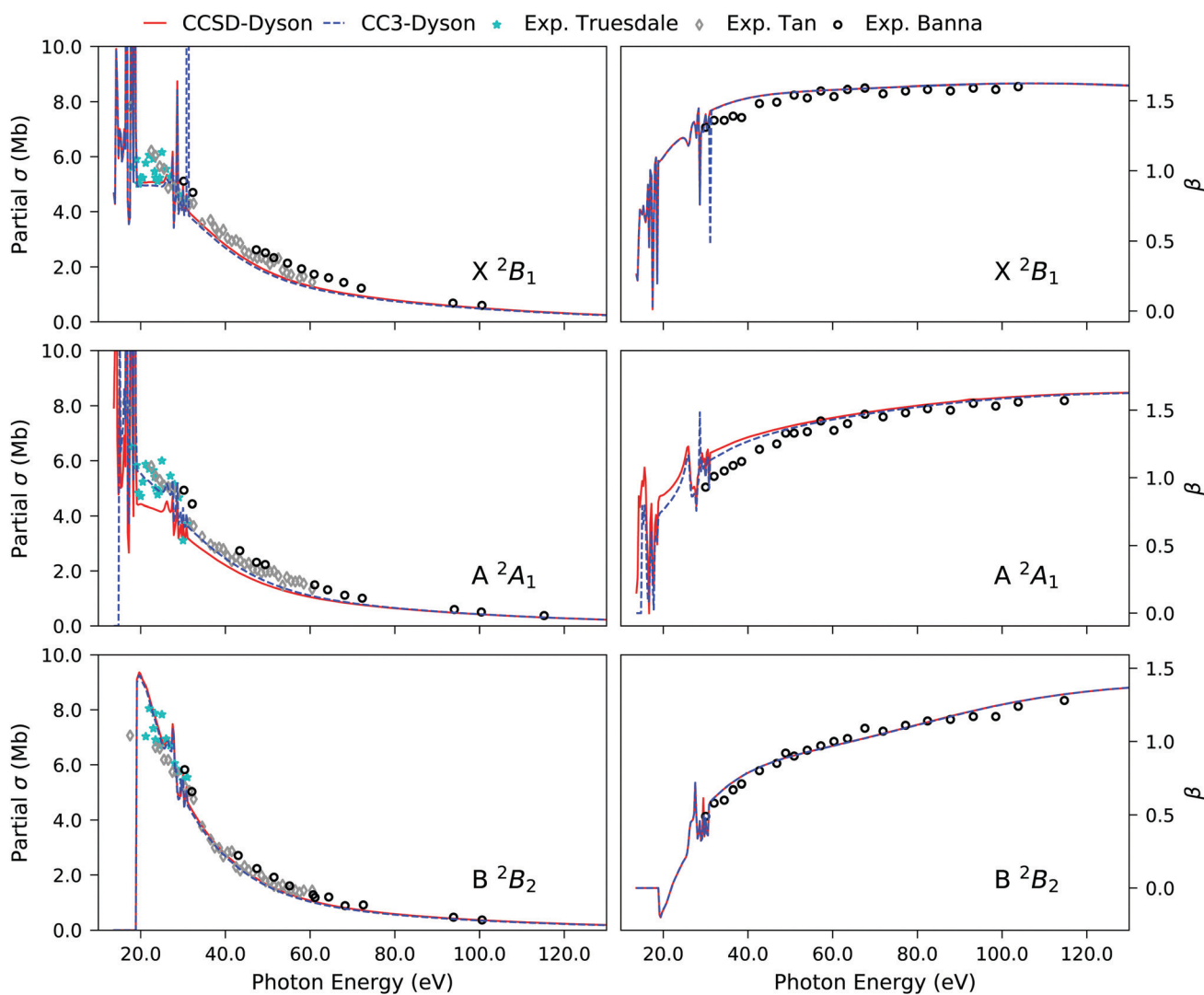

Fig. 2 H_2O. Partial cross-section σ (left panels) and asymmetry parameter β (right panels) for the primary ionization channels obtained using EOM-CCSD and EOM-CC3 Dyson orbital descriptions of the bound state. B-spline TD-DFT is used for the continuum orbital description. Experimental results are taken from ref. 90–92.

This journal is © the Owner Societies 2022

Phys. Chem. Chem. Phys., 2022, **24**, 8329–8343 | **8335**

Table 2 CS. Comparison of Koopmans' theorem Hartree–Fock (HF) molecular orbital energies, EOM-CCSD and EOM-CC3 ionization energies (IE), percentage of singles character (%$|R_1|$), and spectral strengths (R_F) obtained using the aug-cc-pVTZ basis set. All energies are reported in eV. Experimental results are taken from ref. 93. The corresponding photoelectron spectrum is shown in Fig. S2 (ESI). The "major MO" is the orbital contributing the most to the Dyson orbital. The HF electronic configuration for the ground state is $1\sigma^2 2\sigma^2 3\sigma^2 4\sigma^2 1\pi^4 5\sigma^2 6\sigma^2 7\sigma^2 2\pi^4$

		HF	EOM-CCSD			EOM-CC3			Exp[93]
Peak	Major MO	IE	IE (%$\|R_1\|$)	R_F	Dominant amplitude	IE (%$\|R_1\|$)	R_F	Dominant amplitude	IE
X $^2\Sigma$	7σ	12.82	11.52 (96)	0.8672	$7\sigma^{-1}$	11.29 (94)	0.8330	$7\sigma^{-1}$	11.33
A $^2\Pi$	2π	12.60	13.06 (98)	0.9091	$2\pi^{-1}$	12.94 (97)	0.8812	$2\pi^{-1}$	12.79
B $^2\Sigma$			17.26 (90)	0.7683	$6\sigma^{-1}$	16.54 (67)	0.4093	$6\sigma^{-1}$, $2\pi^{-1}(7\sigma^{-1}3\pi)$	15.84
C $^2\Sigma$	6σ	18.83	20.32 (37)	0.1056	$6\sigma^{-1}$, $2\pi^{-1}(7\sigma^{-1}3\pi)$	18.40 (73)	0.4000	$6\sigma^{-1}$, $2\pi^{-1}(7\sigma^{-1}3\pi)$	18.0

primary $(2a_1)^{-1}$ band is overestimated while that of the second, satellite peak is underestimated.

Due to the inclusion of approximate triple excitations at the EOM-CC3 level, the description of 2h1p states is significantly improved. This results in reduced ionization energies for these states. Therefore, there appear multiple satellite states in the high energy region of the spectrum, not only of $(2a_1)^{-1}$ character. The photoelectron spectrum in the inner valence region is not well resolved, and is rather a broad feature, see Fig. 1. Thus, it is reasonable that it envelopes numerous low intensity peaks. The
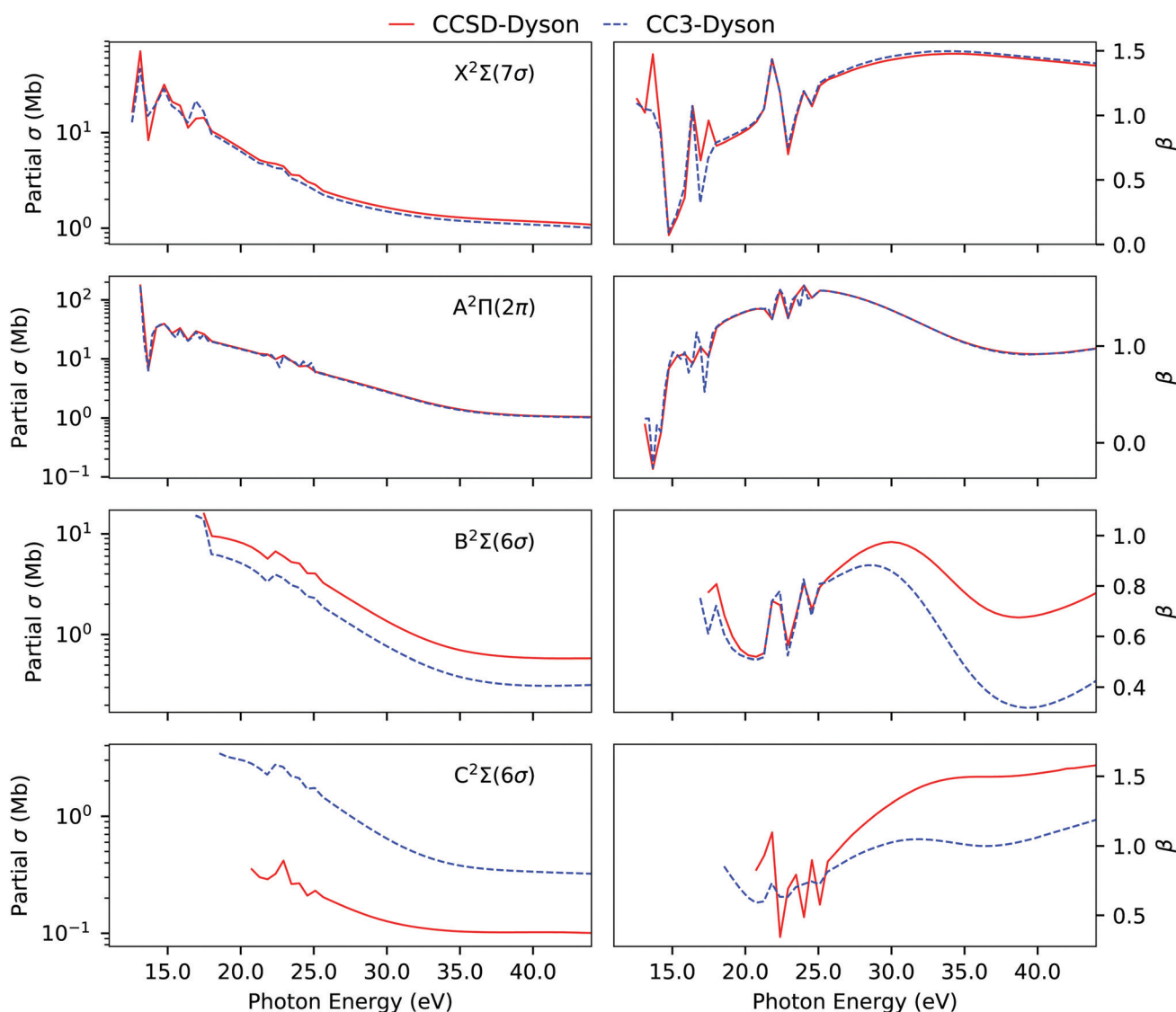

Fig. 3 CS. Partial cross section and asymmetry parameters computed using EOM-CCSD and EOM-CC3 Dyson orbitals with the B-spline TD-DFT continuum description. Basis set aug-cc-pVTZ.

8336 | *Phys. Chem. Chem. Phys.*, 2022, **24**, 8329–8343

This journal is © the Owner Societies 2022

Table 3 H$_2$S. Ionization energies (IE, in eV) and intensities computed using EOM-CCSD and EOM-CC3/aug-cc-pVTZ. Experimental results are taken from ref. 94 and 95. The "major MO" is the orbital contributing the most to the Dyson orbital. The HF ground-state configuration is $1a_1^2 2a_1^2 1b_2^2 3a_1^2 1b_1^2 4a_1^2 2b_2^2 5a_1^2 2b_1^2$

Peak	Major MO	EOM-CCSD			EOM-CC3			Exp[94]	Exp[95]	
		IE (%|R_1|)	R_F	Dominant ampl.	IE (%|R_1|)	R_F	Dominant ampl.	IE	IE	Intensity
X $^2B_1$	$2b_1$	10.42 (98)	0.9291	$2b_1^{-1}$	10.38 (98)	0.9051	$2b_1^{-1}$	10.5	10.50	
A $^2A_1$	$5a_1$	13.43 (98)	0.9128	$5a_1^{-1}$	13.40 (97)	0.8935	$5a_1^{-1}$	13.4	13.10	
B $^2B_2$	$2b_2$	15.69 (98)	0.9141	$2b_2^{-1}$	15.64 (97)	0.8927	$2b_2^{-1}$	15.6	15.60	
	$2b_2$	21.98 (4)	0.0019	$2b_1^{-2}5b_2$, $2b_1^{-2}4b_2$	19.35 (7)	0.0047	$2b_1^{-2}5b_2$, $2b_1^{-2}4b_2$		18	0.018
	$4a_1$	22.41 (68)	0.4130	$4a_1^{-1}$, $2b_1^{-2}9a_1$	20.29 (28)	0.0709	$4a_1^{-1}$, $2b_1^{-2}9a_1$, $2b_1^{-2}8a_1$, $2b_1^{-2}6a_1$	20	19.9	0.059
	$4a_1$	24.35 (54)	0.2617	$4a_1^{-1}$, $2b_1^{-2}8a_1$	22.27 (50)	0.2268	$4a_1^{-1}$, $2b_1^{-2}6a_1$	22.1	22.08	0.210
	$2b_1$				22.62 (2)	0.0007	$2b_1^{-1}(5a_1^{-1}8a_1)$, $2b_1^{-1}(5a_1^{-1}6a_1)$, $2b_1^{-1}(5a_1^{-1}9a_1)$	22.7	22.68	0.060
	$4a_1$	26.26 (17)	0.0232	$2b_1^{-2}9a_1$, $2b_1^{-2}6a_1$	23.26 (34)	0.1026	$4a_1^{-1}$, $2b_1^{-2}10a_1$	23.05	23.00	0.030
	$4a_1$				23.72 (41)	0.1576	$4a_1^{-1}$, $2b_1^{-2}10a_1$	23.31	23.43	0.190

energy region between 26.09 eV and 30.80 eV consists of multiple very low intensity satellites of $(1b_1)^{-1}$, $(3a_1)^{-1}$ $(1b_2)^{-1}$, the total intensity of these peaks being approximately 0.12. The first ionized state of contribution from $(2a_1)^{-1}$ ionization arises at 31.93 eV. The peaks between 31–34 eV and 34–37 eV have an overall spectral intensity of about 0.56 and 0.18, which is in excellent agreement with the experimental monopole strengths of 0.58 and 0.18,[89] respectively.

The photoionization observables for the primary peaks, generated using the B-spline TD-DFT continuum orbitals and the EOM-CCSD and EOM-CC3 Dyson orbitals for the bound part, are shown in Fig. 2. They are indistinguishable, when comparing the two CC methods. This is also reasonable given that even at the EOM-CCSD level, the agreement with the experimental results is quite accurate, not leaving much scope for improvement. However, a slight variance is noticed for the A $^2A_1$ band (middle row in Fig. 2) near the ionization threshold. The partial cross-section computed using EOM-CC3 Dyson orbitals clearly is a better match with the experimental observations. The sharp features obtained in the near-threshold region are due to autoionization resonances, which are not seen in the experiment due to vibrational motion. The features are attributed to discrete excitations to Rydberg states lying in the electronic continuum of the lowest-energy ionization channel. The partial cross-section and asymmetry parameters for the $2a_1^{-1}$ region are shown in Fig. S1 (ESI†).

4.2 Carbon monosulphide

The CS molecule is a favourite test case for theory due to the presence of experimentally well characterized primary and satellite peaks. The experimental photoelectron spectrum of CS exhibits four well separated peaks between 10–18 eV.[93] The calculated ionization energies are listed in Table 2. The two lowest-energy spectral peaks are assigned to ionizations from the HOMO (7σ) and HOMO−1 (2π) molecular orbitals, respectively. As they are dominantly 1h type ionizations, the Dyson orbitals are essentially equivalent to the corresponding molecular orbitals as predicted by Koopmans' theorem.

In CS, the complexity arises in accurately simulating the third and fourth peak. They both originate due to $(6\sigma)^{-1}$ transition. The 6σ Hartree–Fock molecular orbital energy is 18.83 eV, significantly

higher than the third experimental ionization energy (15.84 eV), but comparable to the fourth one at 18.0 eV. The Koopmans description is clearly failing for CS. At the EOM-CCSD level, the two 6σ peaks are captured but at much higher energy and with a larger separation of 3.06 eV between them, in contrast to an experimental gap of 2.16 eV. Furthermore, experimentally the intensities of the third and fourth bands are comparable, whereas, at the CCSD level, the third has a much larger spectral strength than the fourth one. EOM-CC3 significantly improves the ionization energies as well as the intensity distribution between the third and fourth peak (see Fig. S2, ESI†). As also shown in Table 2 and Table S4 (ESI†), considerable differences exist in the singles character and in the dominant amplitudes of the last two ionized states at the CCSD and CC3 levels.

Fig. 4 H$_2$S: right Dyson orbitals for the satellite states computed using EOM-CC3/aug-cc-pVTZ. The first row is plotted with isovalue 0.1, the second row with isovalues 0.01, 0.03 and 0.05, respectively, and the third row with isovalues 6×10^{-3}, 0.05, 0.05. The molecular orbitals corresponding to the X, A and B bands according to Koopmans' theorem are plotted in Fig. S4 (ESI†).

In line with our findings for H_2O, we observe that CC3 allows for more redistribution of spectral intensities from the primary to the satellite peaks, thereby reducing the R_F values of the primary Dyson orbitals in comparison to the CCSD values. A comparison of the photoionization observables computed using EOM-CCSD and EOM-CC3 Dyson orbitals is presented in Fig. 3. The overall spectral shape is the same for the primary ionization bands (X and A). Significantly different partial cross sections and asymmetry parameters have been obtained for the B $^2\Sigma$ and C $^2\Sigma$ band using the CCSD and CC3 Dyson orbitals. We note however that it is difficult to further comment on the correctness of the bound state description for the B $^2\Sigma$ and C $^2\Sigma$ band due to lack of experimental observations to corroborate our findings. The overall asymmetry parameter profiles for the B and C bands are distinct, indicating differences in the nature of the underlying transitions. This also aligns with the findings reported in ref. 5, obtained using CASSCF Dyson orbitals for the description of the bound part.

4.3 Hydrogen sulphide

The computed EOM-CC3/aug-cc-pVTZ photoelectron spectral data of H_2S are listed in Table 3, together with EOM-CCSD/aug-cc-pVTZ data. HF results are reported in Table S8 (ESI†), along with CCSD and CC3 results with a smaller basis set. The experimental spectrum[94] is split into two parts, an outer valence region between 10–17 eV and an inner valence region above 19 eV characterized by low intensity, closely-spaced, peaks. The photoelectron spectrum of the inner valence region is shown in Fig. S5 (ESI†).

The primary ionization features are due to ionization from the $2b_1$, $5a_1$ and $2b_2$ molecular orbitals, which are plotted in Fig. S4 (ESI†). The corresponding Dyson orbitals of these three ionizations resemble the molecular orbitals, with dominant contributions from the central sulphur atom, as shown in Fig. 4, in the order of X > A > B, as previously discussed.[45,94] The Dyson orbital of the X band is a pure

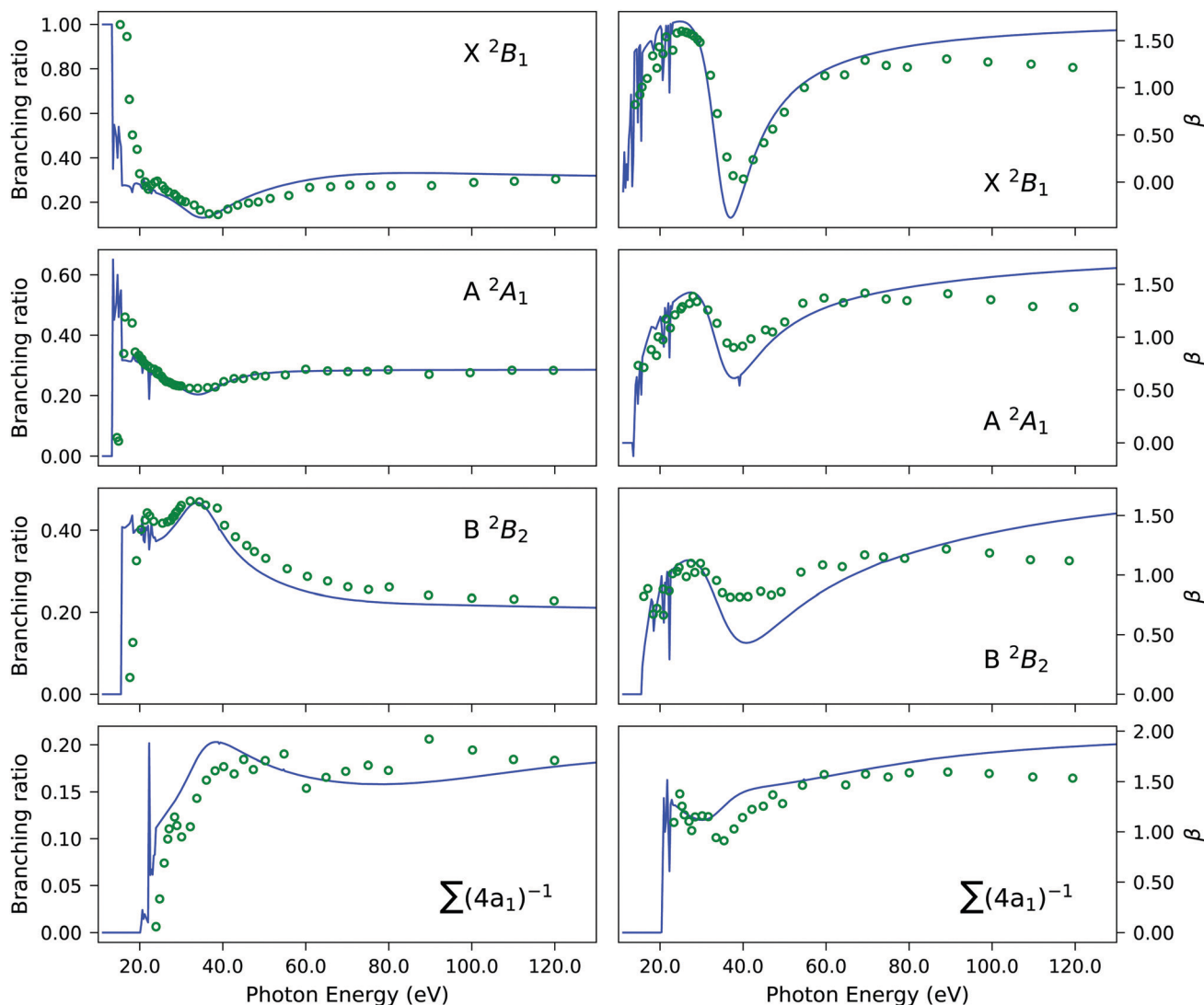Fig. 5 H_2S. Branching ratio (left panels) and asymmetry parameter β (right panels) obtained using the EOM-CC3/aug-cc-pVTZ Dyson orbital description of the bound state with the B-spline TD-DFT continuum (solid blue line) versus experiment (green circles). The summation in the bottom panels refers to the four $4a_1$ states listed in Table 3. The experimental results were re-digitized from ref. 94.

8338 | *Phys. Chem. Chem. Phys.*, 2022, **24**, 8329–8343

This journal is © the Owner Societies 2022

Table 4 CS$_2$. Ionization energies (in eV) and pole strengths computed using EOM-CCSD and EOM-CC3 with the aug-cc-pVDZ basis set. Experimental results are taken from ref. 96. The corresponding photoelectron spectrum is shown in Fig. S7. HF ground state configuration $1\sigma_u^2 1\sigma_g^2 2\sigma_g^2 2\sigma_u^2 3\sigma_g^2 3\sigma_u^2 4\sigma_g^2 1\pi_g^4$ $1\pi_u^4 5\sigma_g^2 4\sigma_u^2 6\sigma_g^2 5\sigma_u^2 2\pi_u^4 2\pi_g^4$

	Major	EOM-CCSD			EOM-CC3			Exp
Peak	MO	IE (%$\|R_1\|$)	R_F	Dominant ampl.	IE (%$\|R_1\|$)	R_F	Dominant ampl.	IE[96]
X $^2\Pi_g$	$2\pi_g$	9.90 (98)	0.8970	$2\pi_g^{-1}$	9.84 (97)	0.8630	$2\pi_g^{-1}$	10.1
A $^2\Pi_u$	$2\pi_u$	13.20 (93)	0.8250	$2\pi_u^{-1}$	12.74 (86)	0.6993	$2\pi_u^{-1}, 2\pi_g^{-2}3\pi_u$	12.9
B $^2\Sigma_u$	$5\sigma_u$	14.45 (96)	0.8734	$5\sigma_u^{-1}$	14.20 (94)	0.8240	$5\sigma_u^{-1}$	14.6
$^2\Pi_u$	$2\pi_u$	17.78 (14)	0.0136	$2\pi_g^{-2}3\pi_u$	14.74 (23)	0.0290	$2\pi_g^{-2}3\pi_u$	
$^2\Pi_u$	$2\pi_u$				15.82 (8)	0.0056	$2\pi_g^{-2}3\pi_u$	
C $^2\Sigma_g$	$6\sigma_g$	16.42 (93)	0.8140	$6\sigma_g^{-1}$	15.93 (86)	0.6798	$6\sigma_g^{-1}$	16.2
D $^2\Pi_u$	$2\pi_u$	21.68 (32)	0.0573	$2\pi_u^{-1}, 2\pi_g^{-2}3\pi_u$	17.60 (43)	0.1480	$2\pi_u^{-1}, 2\pi_g^{-2}3\pi_u$	17.2

S(3p) lone-pair orbital, orthogonal to the molecular plane. That of the B band is of S–H σ bonding type. Ionizations from 3p atomic orbitals of third row elements are known to exhibit Cooper minima at around 40 eV. The depth of the minimum in the asymmetry parameter of the first three bands, shown in Fig. 5, correlates with the extent of the contribution from the sulphur 3p orbital to the Dyson orbital. The X band, having the deepest minimum, has the largest contribution from the S(3p) orbital, while the B band exhibits, amongst the three, the smallest contribution and the most shallow minimum.

Experimentally, the inner valence region is attributed to ionizations from the 4a$_1$ molecular orbital. Our CC3 calculations reveal six ionization channels in this energy span, of which four have 4a$_1$, one 2b$_1$ and one 2b$_2$ as major contributors to the Dyson orbital.

The Dyson orbitals are shown in Fig. 4. As the satellites have pronounced 2h1p excitation character, the schematic representation of the Dyson orbitals of 4a$_1$ molecular orbital parentage does not have an unambiguous one-to-one correspondence to the dominant molecular orbital. In the bottom panels of Fig. 5, the branching ratio and asymmetry parameter for the composite ionization channels arising from the 4a$_1$ molecular orbital have been reported. Here, we do not take into consideration the very weak satellite states of B_1 and B_2 symmetry, as the experimental results (green dots) are for 4a$_1$ ionization channels. For the asymmetry parameter of the individual satellite ionization channels, see Fig. S6 (ESI†). The minimum in the asymmetry parameter β is computed to be at a slightly lower photon energy, and the depth of the minimum is underestimated, as shown in the bottom right panel of Fig. 5. The experimental branching ratio for the satellite state shows oscillations above 60 eV. On the contrary, our simulations produce an almost flat structure. This is reasonable as we have only taken into account ionizations up to 25 eV, thereby neglecting contributions from all higher-energy ionization channels.

4.4 Carbon disulphide

The computed and experimental ionization energies and spectral strengths of CS$_2$ are reported in Table 4 and Table S9 (ESI†). The four outermost primary ionizations are simple and already well described at the EOM-CCSD level.[45] Here, we focus on the

fifth band, which has been experimentally characterized to be of $^2\Pi_u$ symmetry. According to Koopmans' theorem, the fifth band should be due to pure ionization from the 4σ$_u$ orbital, which, on the other hand, has a much higher ionization energy. Even though at the EOM-CCSD level we do obtain an ionization at 17.78 eV, which is comparable to the experimental position, its intensity is significantly underestimated. This is also translated to the partial cross-section, which is also underestimated

Fig. 6 CS$_2$. Individual channel photoionization cross-section σ and asymmetry parameter β of the D band computed using B-spline TD-DFT continuum orbitals with Dyson orbitals computed using the aug-cc-pVDZ basis set. The experimental results (green dots) are from ref. 96. The CCSD results were also reported in ref. 45, together with CCSDR(3) corrected counterparts.

by an order of magnitude in comparison to experiment, as shown in Fig. 6. However, an appreciable agreement is seen for the asymmetry parameter due to the correct symmetry of the underlying transition. An earlier analysis of the ionization vector also revealed that the CCSD ionization at 17.78 eV has exclusively double excitation character, so we expect it to move significantly upon inclusion of triple excitations.[45] Another $2\Pi_u$ state is obtained at 21.68 eV, with a sizeable amount of single excitation character.

Indeed, using EOM-CC3, the ionization energy is considerably lowered from 17.78 eV to 14.74 eV, and the other $2\Pi_u$ satellite at 21.68 eV moves down to 17.60 eV. While the ionization energy of this latter peak is still overestimated, the agreement with the fifth band of the experiment is substantially improved. The photoionization cross-section and asymmetry parameter computed using this 21.68 eV EOM-CCSD Dyson

orbital provide a good match with experiment. However, in case of the asymmetry parameter, it is difficult to comment on the performance of the Dyson orbital treatment as the experimental results are scattered.

4.5 Methyloxirane

As final example, Fig. 7 illustrates the results of our approach for the photoelectron circular dichroic parameter, β_1, of (*S*)-methyloxirane, a prototypical chiral molecule. We study the six lowest-energy ionization channels, which are characterized as ionization from one particular molecular orbital. The computed photoelectron spectral details are reported in Table S10 (ESI†). The corresponding EOM-CC3 Dyson orbitals are shown in Fig. S11 (ESI†). It has been shown previously,[27] that Koopmans' theorem-based Hartree–Fock molecular orbitals fail to reproduce the experimental trends in the near-threshold

Fig. 7 C_3H_6O: photoelectron circular dichroic parameter β_1 computed using EOM–CC3/aug–cc–pVTZ Dyson orbitals and B–spline TD–DFT continuum orbitals, shown by blue lines. Experimental results (green dots) were taken from ref. 97. The spectral features are convoluted using Gaussian broadening of full width at half maximum of 1.0 eV.

8340 | *Phys. Chem. Chem. Phys.*, 2022, **24**, 8329–8343

This journal is © the Owner Societies 2022

region. Here, we see that our combined method matches the experimental data well. Not surprisingly, since all six channels correspond to primary ionizations, the CC3 and CCSD results are very similar, as it can be appreciated from Fig. S12 (ESI†). Also, static DFT and TD-DFT representations of the continuum yield photoelectron dichroic parameters of similar quality, as seen in Fig. S12 (ESI†).

5 Conclusions

In summary, we have devised a technique combining EOM-CC3 Dyson orbital coefficients to describe the bound state character of the system with B-spline TD-DFT continuum orbitals, allowing for the accurate simulation of photoelectron spectra and photoionization dynamical observables, namely partial cross-sections, asymmetry parameters, branching ratios and photoelectron dichroic parameters. The study involved two main components, the implementation of the EOM-CC3 Dyson orbital coefficients and their interface with the B-spline (TD-)DFT continuum for the computation of the spectroscopic parameters.

A detailed investigation of the outer as well as inner valence region of the photoelectron spectrum of exemplary molecular systems has been carried out. For outer valence ionizations, CCSD results are already accurate, and CC3 brings little improvement. The accuracy of CCSD may be gauged by the pole strengths R_F of the individual ionizations, and the percentage of 1h states. As a rule of thumb, CCSD results may be considered accurate when $R_F > 0.85$ and the 1h-percentage >0.90.

The perturbative triples correction is necessary for reproducing complex satellite bands of higher order excitation character. The inner valence region of the spectrum comprising satellite peaks is a direct probe of correlation effects and quite challenging to accurately reproduce theoretically. Recent developments in experimental facilities have made it possible to capture such low intensity features with high accuracy, giving impetus to concomitant theoretical advancements. Even though EOM-CCSD is capable of describing 2h1p ionizations, the ionization energy is often highly overestimated making it difficult to assign the ionized states to the corresponding experimental bands. This is extensively corrected at the EOM-CC3 level. The proposed EOM-CC3 Dyson orbital treatment of the bound state in conjunction with B-spline TD-DFT continuum orbitals constitutes a state-of-the-art theoretical methodology capable of quantitative comparison with experiments.

The presented protocol is general and can be extended and applied to investigate sophisticated experimental observations. For instance, open-shell systems could be studied using the method. Core ionization spectra will also be studied in the future, as they are known to exhibit a plethora of satellite peaks, difficult to handle using only singles and doubles excitations. The method can also be suitably extended to include nuclear dynamic effects, in order to describe vibrationally resolved photoelectron spectral features.

Author contributions

Conflicts of interest

There are no conflicts to declare.

Acknowledgements

References

1 F. Merkt, S. Willitsch and U. Hollenstein, High-resolution Photoelectron Spectroscopy, in *Handbook of High-resolution Spectroscopy*, ed. M. Quack and F. Merkt, John Wiley & Sons, Ltd, 2011.

2 M. Nisoli, P. Decleva, F. Calegari, A. Palacios and F. Martín, *Chem. Rev.*, 2017, **117**, 10760–10825.

3 R. L. Martin and D. A. Shirley, *J. Chem. Phys.*, 1976, **64**, 3685–3689.

4 L. S. Cederbaum, W. Domcke, J. Schirmer and W. Von Niessen, *Adv. Chem. Phys.*, 1986, **65**, 115–159.

5 A. Ponzi, C. Angeli, R. Cimiraglia, S. Coriani and P. Decleva, *J. Chem. Phys.*, 2014, **140**, 204304.

6 A. Ponzi, N. Quadri, C. Angeli and P. Decleva, *Phys. Chem. Chem. Phys.*, 2019, **21**, 1937–1951.

7 L. S. Cederbaum, J. Schirmer, W. Domcke and W. von Niessen, *J. Phys. B: At. Mol. Phys.*, 1977, **10**, L549–L553.

8 L. S. Cederbaum, J. Schirmer, W. Domcke and W. Von Niessen, *Int. J. Quantum Chem.*, 1978, **14**, 593–601.

9 D. Danovich, *Wiley Interdiscip. Rev.: Comput. Mol. Sci.*, 2011, **1**, 377–387.

10 W. von Niessen, J. Schirmer and L. S. Cederbaum, *Comput. Phys. Rep.*, 1984, **1**, 57–125.

11 J. Schirmer, A. B. Trofimov and G. Stelter, *J. Chem. Phys.*, 1998, **109**, 4734–4744.

12 A. B. Trofimov and J. Schirmer, *J. Chem. Phys.*, 2005, **123**, 144115.

This journal is © the Owner Societies 2022

Phys. Chem. Chem. Phys., 2022, **24**, 8329–8343 | **8341**

13 J. V. Ortiz, *Adv. Quantum Chem.*, Academic Press, 1999, vol. 35, pp. 33–52.

14 E. Opoku, F. Pawłowski and J. V. Ortiz, *J. Chem. Phys.*, 2021, **155**, 204107.

15 M. Ehara, M. Ishida and H. Nakatsuji, *J. Chem. Phys.*, 2001, **114**, 8990–8999.

16 Q. Tian, J. Yang, Y. Shi, X. Shan and X. Chen, *J. Chem. Phys.*, 2012, **136**, 094306.

17 A. D. O. Bawagan and E. R. Davidson, *Adv. Chem. Phys.*, 1999, **110**, 215–263.

18 B. O. Roos, *Adv. Chem. Phys.*, 1987, 399–445.

19 K. Andersson, P. Malmqvist and B. O. Roos, *J. Chem. Phys.*, 1992, **96**, 1218–1226.

20 P.-Å. Malmqvist, K. Pierloot, A. R. M. Shahi, C. J. Cramer and L. Gagliardi, *J. Chem. Phys.*, 2008, **128**, 204109.

21 V. Sauri, L. Serrano-Andrés, A. R. M. Shahi, L. Gagliardi, S. Vancoillie and K. Pierloot, *J. Chem. Theory Comput.*, 2011, **7**, 153–168.

22 G. Grell, S. Bokarev, B. Winter, R. Seidel, E. Aziz, S. Aziz and O. Kühn, *J. Chem. Phys.*, 2015, **143**, 074104.

23 G. Grell and S. I. Bokarev, *J. Chem. Phys.*, 2020, **152**, 074108.

24 B. N. C. Tenorio, A. Ponzi, S. Coriani and P. Decleva, *Molecules*, 2022, **27**, 1203.

25 C. M. Oana and A. I. Krylov, *J. Chem. Phys.*, 2007, **127**, 234106.

26 S. Gozem, A. O. Gunina, T. Ichino, D. L. Osborn, J. F. Stanton and A. I. Krylov, *J. Phys. Chem. Lett.*, 2015, **6**, 4532–4540.

27 T. Moitra, A. Ponzi, H. Koch, S. Coriani and P. Decleva, *J. Phys. Chem. Lett.*, 2020, **11**, 5330–5337.

28 M. L. Vidal, A. I. Krylov and S. Coriani, *Phys. Chem. Chem. Phys.*, 2020, **22**, 2693–2703.

29 M. L. Vidal, A. I. Krylov and S. Coriani, *Phys. Chem. Chem. Phys.*, 2020, **22**, 3744–3747.

30 H. Koch and P. Jørgensen, *J. Chem. Phys.*, 1990, **93**, 3333–3344.

31 H. Koch, H. J. A. Jensen, P. Jørgensen and T. Helgaker, *J. Chem. Phys.*, 1990, **93**, 3345–3350.

32 J. F. Stanton and R. J. Bartlett, *J. Chem. Phys.*, 1993, **98**, 7029–7039.

33 A. I. Krylov, *Annu. Rev. Phys. Chem.*, 2008, **59**, 433–462.

34 S. Coriani, F. Pawłowski, J. Olsen and P. Jørgensen, *J. Chem. Phys.*, 2016, **144**, 024102.

35 R. J. Bartlett, *Wiley Interdisc. Rev.: Comput. Mol. Sci.*, 2012, **2**, 126–138.

36 H. Koch, O. Christiansen, P. Jørgensen, A. M. Sanchez de Merás and T. Helgaker, *J. Chem. Phys.*, 1997, **106**, 1808–1818.

37 O. Christiansen, H. Koch and P. Jørgensen, *J. Chem. Phys.*, 1996, **105**, 1451–1459.

38 O. Christiansen, H. Koch and P. Jørgensen, *J. Chem. Phys.*, 1995, **103**, 7429–7441.

39 R. H. Myhre and H. Koch, *J. Chem. Phys.*, 2016, **145**, 044111.

40 A. C. Paul, R. H. Myhre and H. Koch, *J. Chem. Theory Comput.*, 2021, **17**, 126.

41 J. V. Ortiz, *J. Chem. Phys.*, 2020, **153**, 070902.

42 A. I. Krylov, *J. Chem. Phys.*, 2020, **153**, 080901.

43 M. Díaz-Tinoco, H. H. Corzo, F. Pawłowski and J. V. Ortiz, *Mol. Phys.*, 2019, **117**, 2275–2283.

44 V. Pomogaev, S. Lee, S. Shaik, M. Filatov and C. H. Choi, *J. Phys. Chem. Lett.*, 2021, **12**, 9963–9972.

45 T. Moitra, S. Coriani and P. Decleva, *J. Chem. Theory Comput.*, 2021, **17**, 5064–5079.

46 T. Fukumi, *J. Chem. Phys.*, 1981, **75**, 3743–3745.

47 F. Müller-Plathe and G. H. Diercksen, Molecular photoionisation cross sections by moment theory. An introduction, in *Electronic Structure of Atoms, Molecules and Solids. Proceeding of the II Escola Brasileira de Estructure Eletronica, Olinda, Brazil, July 17–22, 1989*, ed. S. Canuto, J. D'Albuquerque e Castro and F. J. Paixao, World Scientific, Olinda, Brazil, 1990, pp. 1–29.

48 J. Cukras, S. Coriani, P. Decleva, O. Christiansen and P. Norman, *J. Chem. Phys.*, 2013, **139**, 094103.

49 J. Cukras, P. Decleva and S. Coriani, *J. Chem. Phys.*, 2014, **141**, 174315.

50 B. N. C. Tenorio, M. A. C. Nascimento, S. Coriani and A. B. Rocha, *J. Chem. Theory Comput.*, 2016, **12**, 4440–4459.

51 B. N. C. Tenorio, T. Moitra, M. A. C. Nascimento, A. B. Rocha and S. Coriani, *J. Chem. Phys.*, 2019, **150**, 224104.

52 B. N. C. Tenorio, S. Coriani, A. B. Rocha and M. A. C. Nascimento, Photoionization and Photodetachment Cross Sections Based on L^2 Basis Sets: Theory and Selected Examples, in *Advances in Methods and Applications of Quantum Systems in Chemistry, Physics, and Biology*, ed. A. V. Glushkov, O. Y. Khetselius, J. Maruani and E. Brändas, Springer International Publishing, Springer, 2021, pp. 151–179.

53 S. P. Neville, V. Averbukh, M. Ruberti, R. Yun, S. Patchkovskii, M. Chergui, A. Stolow and M. S. Schuurman, *J. Chem. Phys.*, 2016, **145**, 144307.

54 T. Moitra, S. Coriani and B. N. C. Tenorio, *Mol. Phys.*, 2021, e1980235.

55 P. G. Burke, *R-matrix theory of atomic collisions: application to atomic, molecular and optical processes*, Springer, 2011.

56 Z. Mašín, J. Benda, J. D. Gorfinkiel, A. G. Harvey and J. Tennyson, *Comput. Phys. Commun.*, 2020, **249**, 107092.

57 M. B. Amar and F. C. Farnoux, *J. Phys. B: At. Mol. Phys.*, 1983, **16**, 2339–2358.

58 R. R. Lucchese, K. Takatsuka and V. McKoy, *Phys. Rep.*, 1986, **131**, 147–221.

59 T. N. Rescigno, C. W. McCurdy, A. E. Orel and B. H. Lengsfield, in *The Complex Kohn Variational Method*, ed. W. M. Huo and F. A. Gianturco, Springer US, Boston, MA, 1995, pp. 1–44.

60 M. Brosolo, P. Decleva and A. Lisini, *Chem. Phys.*, 1994, **181**, 85–95.

61 C. F. Fischer and M. Idrees, *J. Phys. B: At., Mol. Opt. Phys.*, 1990, **23**, 679–691.

62 P. V. Demekhin, A. Ehresmann and V. L. Sukhorukov, *J. Chem. Phys.*, 2011, **134**, 024113.

63 D. Toffoli, M. Stener, G. Fronzoni and P. Decleva, *Chem. Phys.*, 2002, **276**, 25–43.

64 M. Stener, G. Fronzoni and P. Decleva, *J. Chem. Phys.*, 2005, **122**, 234301.

8342 | *Phys. Chem. Chem. Phys.*, 2022, **24**, 8329–8343

This journal is © the Owner Societies 2022

65 V. P. Majety, A. Zielinski and A. Scrinzi, *New J. Phys.*, 2015, **17**, 063002.

66 C. Marante, M. Klinker, I. Corral, J. González-Vázquez, L. Argenti and F. Martín, *J. Chem. Theory Comput.*, 2017, **13**, 499–514.

67 M. Klinker, C. Marante, L. Argenti, J. González-Vázquez and F. Martín, *J. Phys. Chem. Lett.*, 2018, **9**, 756–762.

68 S. D. Folkestad, E. F. Kjønstad, R. H. Myhre, J. H. Andersen, A. Balbi, S. Coriani, T. Giovannini, L. Goletto, T. S. Haugland, A. Hutcheson, I.-M. Høyvik, T. Moitra, A. C. Paul, M. Scavino, A. S. Skeidsvoll, Å. H. Tveten and H. Koch, *J. Chem. Phys.*, 2020, **152**, 184103.

69 R. Nesbet, *Variational Methods in Electron-Atom Scattering Theory*, Plenum Press, New York, 1980.

70 T. Helgaker, P. Jørgensen and J. Olsen, *Molecular electronic-structure theory*, John Wiley & Sons, Ltd, 2000, pp. 1–908.

71 J. F. Stanton and J. Gauss, *J. Chem. Phys.*, 1999, **111**, 8785.

72 S. Coriani and H. Koch, *J. Chem. Phys.*, 2015, **143**, 181103.

73 J. F. Stanton, *J. Chem. Phys.*, 1994, **101**, 8928–8937.

74 S. V. Levchenko, T. Wang and A. I. Krylov, *J. Chem. Phys.*, 2005, **122**, 224106.

75 D. A. Matthews, J. Gauss and J. F. Stanton, *J. Chem. Theory Comput.*, 2013, **9**, 2567–2572.

76 D. A. Matthews and J. F. Stanton, *J. Chem. Phys.*, 2015, **142**, 064108.

77 C.-h. Yu, R. M. Pitzer and C. W. McCurdy, *Phys. Rev. A: At., Mol., Opt. Phys.*, 1985, **32**, 2134–2141.

78 R. Matsuzaki and S. Yabushita, *J. Comput. Chem.*, 2017, **38**, 2030–2040.

79 A. Ammar, A. Leclerc and L. U. Ancarani, *J. Comput. Chem.*, 2020, **41**, 2365–2377.

80 M. Stener, S. Furlan and P. Decleva, *J. Phys. B-At. Mol. Opt.*, 2000, **33**, 1081–1102.

81 C. Froese Fischer and M. Idrees, *Comput. Phys.*, 1989, **3**, 53–58.

82 A. Zangwill and P. Soven, *Phys. Rev. A: At., Mol., Opt. Phys.*, 1980, **21**, 1561–1572.

83 N. Chandra, *J. Phys. B: At. Mol. Phys.*, 1987, **20**, 3405–3415.

84 *NIST Computational Chemistry Comparison and Benchmark Database*, NIST Standard Reference Database Number 101, Release 20 August 2019.

85 D. Di Tommaso, M. Stener, G. Fronzoni and P. Decleva, *ChemPhysChem*, 2006, **7**, 924–934.

86 G. te Velde, F. M. Bickelhaupt, E. J. Baerends, C. Fonseca Guerra, S. J. A. van Gisbergen, J. G. Snijders and T. Ziegler, *J. Comput. Chem.*, 2001, **22**, 931–967.

87 E. Van Lenthe and E. J. Baerends, *J. Comput. Chem.*, 2003, **24**, 1142–1156.

88 E. F. Pettersen, T. D. Goddard, C. C. Huang, E. C. Meng, G. S. Couch, T. I. Croll, J. H. Morris and T. E. Ferrin, *Protein Sci.*, 2021, **30**, 70–82.

89 A. Bawagan, L. Lee, K. Leung and C. Brion, *Chem. Phys.*, 1985, **99**, 367–382.

90 K. H. Tan, C. E. Brion, P. E. V. der Leeuw and M. J. van der Wiel, *Chem. Phys.*, 1978, **29**, 299–309.

91 M. S. Banna, B. H. McQuaide, R. Malutzki and V. Schmidt, *J. Chem. Phys.*, 1986, **84**, 4739–4744.

92 C. M. Truesdale, S. Southworth, P. H. Kobrin, D. W. Lindle, G. Thornton and D. A. Shirley, *J. Chem. Phys.*, 1982, **76**, 860–865.

93 N. Jonathan, A. Morris, M. Okuda, K. J. Ross and D. J. Smith, *Faraday Discuss. Chem. Soc.*, 1972, **54**, 48–55.

94 P. Baltzer, L. Karlsson, M. Lundqvist, B. Wannberg, D. M. P. Holland and M. A. MacDonald, *Chem. Phys.*, 1995, **195**, 403–422.

95 M. Y. Adam, A. Naves de Brito, M. P. Keane, S. Svensson, L. Karlsson, E. Källne and N. Correia, *J. Electron Spectrosc. Relat. Phenom.*, 1991, **56**, 241–257.

96 T. A. Carlson, M. O. Krause and F. A. Grimm, *J. Chem. Phys.*, 1982, **77**, 1701–1709.

97 S. Stranges, S. Turchini, M. Alagia, G. Alberti, G. Contini, P. Decleva, G. Fronzoni, M. Stener, N. Zema and T. Prosperi, *J. Chem. Phys.*, 2005, **122**, 244303.